fractal and fractional

MDPI

Article

Experimental Study of Rock Failure and Fractal Characteristics Under True Triaxial Unloading

Chongyan Liu [1,2], Guangming Zhao [1,2], Cheng Pan [3,4,*], Xiangrui Meng [1,2] and Wensong Xu [1,2]

[1] Key Laboratory of Safe and Effective Coal Mining, Ministry of Education of China, Anhui University of Science and Technology, Huainan 232001, China; chongyanliu@126.com (C.L.)
[2] Joint National-Local Engineering Research Centre for Safe and Precise Coal Mining, Anhui University of Science and Technology, Huainan 232001, China
[3] School of Civil Engineering and Architecture, Anhui University of Science and Technology, Huainan 232001, China
[4] School of Civil Engineering, Southeast University, Nanjing 211189, China
* Correspondence: cpan_civil@aust.edu.cn

Abstract: In order to study the failure and fractal characteristics of unloaded rocks, with the help of the true triaxial unloading rock test system and the acoustic emission (AE) monitoring system, rock failure tests were conducted under varying intermediate principal stress and the mechanical response features of the rocks were analyzed. An investigation was conducted into the rocks' AE patterns and multifractal features. The results showed that the rocks' AE macroscopic and microscopic main failure modes differed slightly under unloading. As the intermediate principal stress σ_2 increased, the fractal dimension of the cracks in the rocks first increased and then decreased. The distribution of rock failure was initially concentrated, then dispersed, and concentrated again at the end. As the σ_2 increased, the number of failure events within a specified area in the rock samples under unloading, as represented by the ring-down count, first increased and then decreased. Meanwhile, the fractal dimension $\Delta\alpha$ first decreased and then increased. These results characterized the process whereby the failure distribution pattern of the rocks changed from being concentrated to dispersed and back to concentrated again.

Keywords: true triaxial state; surrounding rocks; acoustic emission; fractal dimension

check for updates

Academic Editors: Lihai Tan, Xiaohan Yang, Gaofeng Liu and Carlo Cattani

Received: 30 January 2025
Revised: 19 February 2025
Accepted: 14 March 2025
Published: 16 March 2025

Citation: Liu, C.; Zhao, G.; Pan, C.; Meng, X.; Xu, W. Experimental Study of Rock Failure and Fractal Characteristics Under True Triaxial Unloading. *Fractal Fract.* **2025**, *9*, 182. https://doi.org/10.3390/fractalfract9030182

Copyright: © 2025 by the authors. Licensee MDPI, Basel, Switzerland. This article is an open access article distributed under the terms and conditions of the Creative Commons Attribution (CC BY) license (https://creativecommons.org/licenses/by/4.0/).

1. Introduction

Unloading is a common phenomenon during the construction of tunnels, side slopes, energy storage facilities, and other civil engineering projects. Cai et al. [1] reported that unloading is the internal driving force behind rock failure. Stress concentration will likely happen after unloading, resulting in rock bursts, rock spalling, and serious deformation. These accidents may cause casualties and economic losses. Understanding the failure mechanism of rocks under true triaxial unloading offers high scientific value from the theoretical, experimental, and engineering perspectives.

Rocks are subjected to a three-directional stress field in the natural environment [2]. However, engineering and theoretical studies tend to simplify the three-dimensional problem into a two-dimensional one and neglect the action of intermediate principal stress [3]. It is inaccurate to analyze rock failure by assuming the presence of conventional triaxial stresses. Mogi et al. were among the first to develop a crude prototype of the true triaxial test system [4], based on which improvements were continuously made until the real true triaxial test system appeared [5]. Unlike the conventional triaxial test system, the true

triaxial test system imposes unequal intermediate and minimum principal stresses on the samples and achieves unloading [6]. Haimson et al. conducted intermediate principal stress tests and suggested that stress σ_2 significantly impacted the rocks' mechanical characteristics, including the strength and deformation [7]. It was found that under true triaxial conditions, intermediate principal stress had a greater influence on the fracture characteristics of rocks than under conventional triaxial stresses. Their CT scan showed that the intermediate principal stress induced fracture in the rocks [8]. The intermediate principal stress enhanced the rocks' bearing capacity and increased the elastic modulus [9]. Takahashi et al. conducted true triaxial tests and found that the intermediate principal stress greatly influenced the rock permeability [10]. Feng et al. performed true triaxial tests in sandstone and granite [11]. The peak stress changed asymmetrically as the intermediate principal stress increased. The anisotropic deformation of the rocks was closely related to the load angle. Chang et al. found that the crack initiation stress decreased as the intermediate principal stress increased and then proposed a rock damage model [12].

The intermediate principal stress, σ_2, not only influences the rock strength but also the rock failure mode and rock burst intensity [13]. Liu et al. confirmed the enhancing effect of the intermediate principal stress on the bearing capacity of granite, facilitating the failure mode transformation of rocks under unloading. Moreover, by theoretical calculation, the intermediate principal stress influenced the rock strength by affecting the intensity factor in the unloading plane. This, in turn, determined the failure mode and failure law of rocks under unloading [14]. Li et al. found in the true triaxial unloading test that the energy storage limit of sandstone decreased as the intermediate principal stress increased [15]. The intermediate principal stress exerted a constraint and acted as a tensile stress. Under true triaxial unloading, σ_2 had a very strong influence on the changes in the rock energy [16]. At a higher σ_2 before unloading, greater elastic strain would accumulate within the samples, leading to higher AE energy upon rock bursts [17]. Thus, σ_2 exerts a huge impact on the rocks' mechanical characteristics, microscopic damage, and energy evolution and, therefore, should not be neglected. However, few studies have considered single-sided unloading in the true triaxial tests.

The fractal theory offers a useful tool for describing the heterogeneity of rock damage. The debris or crack distribution is used to analyze the influence of different principal stresses, lithologies, and load paths on the degree of rock damage [18,19]. Acoustic emission (AE) testing offers an important pathway to characterize rock damage [20]. AE signals are a group of complex, non-linear, non-smooth time series [21]. Analyzing AE signals can reveal rocks' spatial and temporal evolution laws and damage characteristics and inform the assessment of rocks' damage degree and brittle brittleness [22]. Li et al. analyzed the spatial and temporal laws of fractal dimension evolution and the relationship between the fractal dimension and the stress level based on the fractal features of the AE count [23]. Zhao et al. studied the fractal features of AE signals and showed that the ring-down count and the fractal dimension of energy decreased continuously from maximum to minimum [24]. This variation law could be used as the precursory characteristic of rock instability and failure. Zhang et al. proposed a failure analysis approach based on the fractal features of AE signals and suggested that a change in the fractal dimension is a portent of the cracking and failure of an arch dam [25]. The fractal theory opens up a new perspective for the acoustic study of rocks.

More importantly, the multifractal theory uses geometric probability to describe the local singularity of metrics and functions [26]. AE signals can be decomposed by multifractals. Xie et al. introduced the multifractal theory to analyze the waveform multifractal spectra of goaf rock AE signals from AE ground pressure monitoring and identified the variation characteristics of multifractal spectra [27]. Cai et al. analyzed AE signals using

multifractals and found that at different loading stages, the multifractal spectra of the AE signals were characterized by the occurrence of small probability events, which was indicative of the complexity of the rock damage process [28]. Using the multifractal theory, Lu et al. performed a structural analysis of the AE signals generated spontaneously in the coal [29]. The above studies have demonstrated the feasibility of using multifractals to process rock AE signals. There is still a scarcity of multifractal feature analyses of the AE ring-down counts from true triaxial unloading tests.

In the present study, true triaxial unloading tests at different σ_2 values were designed, and the macroscopic and microscopic failure modes of rocks and the fractal dimensions of cracks were analyzed. Two parameters, the ring-down count and cumulative AE energy, were estimated to characterize the rock failure evolution and variabilities at different σ_2 values. Finally, the multifractal theory was employed to obtain the multifractal and the singular spectra of the ring-down counts. Our research findings shed some light on the influence of σ_2 stress on the mechanical characteristics of rocks under unloading in real-world engineering scenarios.

2. Experimental

2.1. Rock Sample Collection

Rock samples were collected from the mines in the Shaanxi Province of China, and large rock masses were picked from the tunneling head of the rail haulage roadway. The rock samples collected were grayish–white and fine- to medium-grained. Tests were performed to quantitatively assess the mechanical properties of the sandstone samples, including the uniaxial compression test, Brazilian splitting test, scanning electron microscopy (SEM), and X-ray diffraction (XRD). Some physical parameters of the rock samples (e.g., wave velocity and density) were also determined. The results are shown in Table 1.

Table 1. Physical parameters of the rock samples.

Density (g/cm^3)	Longitudinal Wave Velocity (m/s)	Porosity	Poisson Ratio	Tensile Strength (MPa)	Uniaxial Compressive Strength (MPa)	Elastic Modulus (GPa)
2.39	2495.52	0.45%	0.27	2.84	35.02	26.8

The sandstone samples comprised quartz, feldspar, dolomite, and clay minerals, whose relative contents were about 60.2%, 12.9%, 11.6%, and 13.2%, respectively. The samples also contained a small amount of hematite. The microscopic morphology of the samples upon SEM is shown in Figure 1.

For the true triaxial unloading tests, one sandstone block was cut into a rectangular prism, whose dimensions were 100 mm × 100 mm × 100 mm. Following the method regulated by the International Society for Rock Mechanics and Rock Engineering (ISRM), the rectangular prism sample was further processed to achieve smooth surfaces [30].

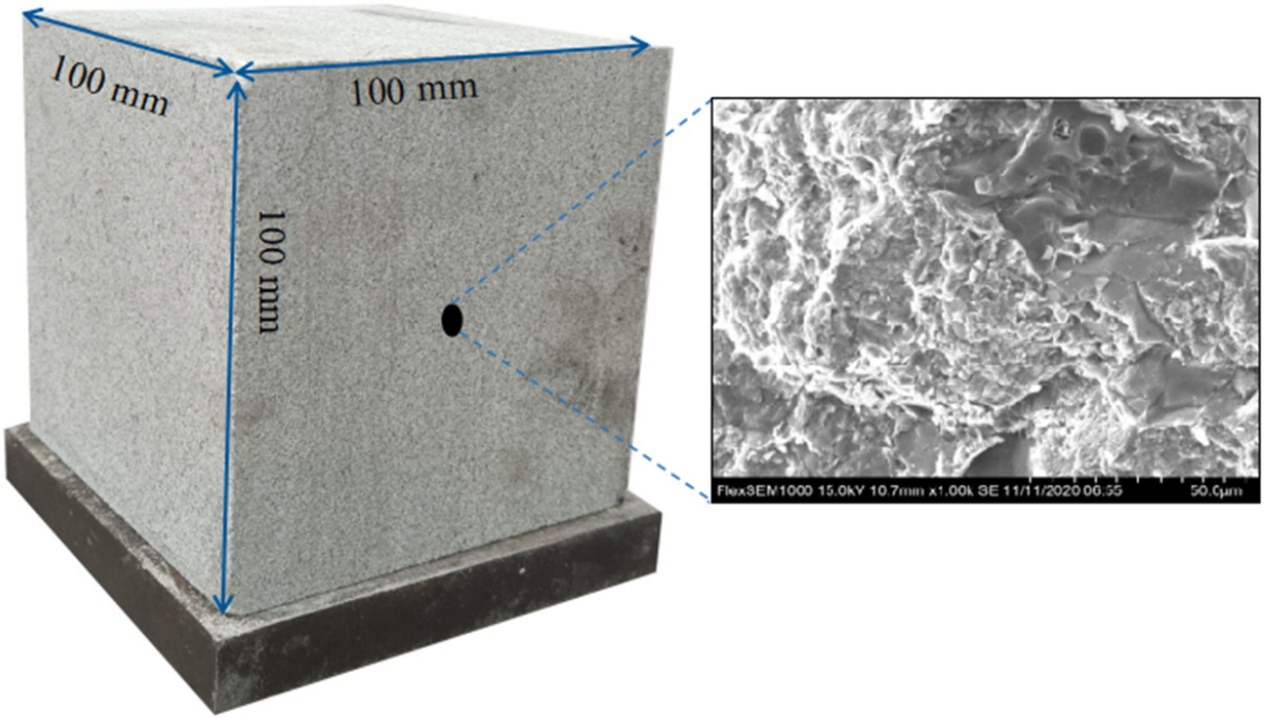

Figure 1. Dimensions and SEM image with microscopic morphology of the rock samples.

2.2. Experimental System

The true triaxial disturbance unloading rock testing system developed by Anhui University of Science and Technology was used for the tests, as shown in Figure 2a. This rigid test apparatus applied stresses in three directions, each servo-controlled independently. Uniaxial, biaxial, true triaxial, single-sided, and double-sided unloading tests were performed using the rigid test apparatus. The maximum stresses applied in the vertical and horizontal directions were 5000 and 3000 kN, respectively. The sample dimensions were adjustable from 100 to 300 mm. The clamp was installed in a staggered manner to adapt to diverse working conditions and help avoid clamp occlusion upon sample deformation. This clamping style also prevented the appearance of blank corners.

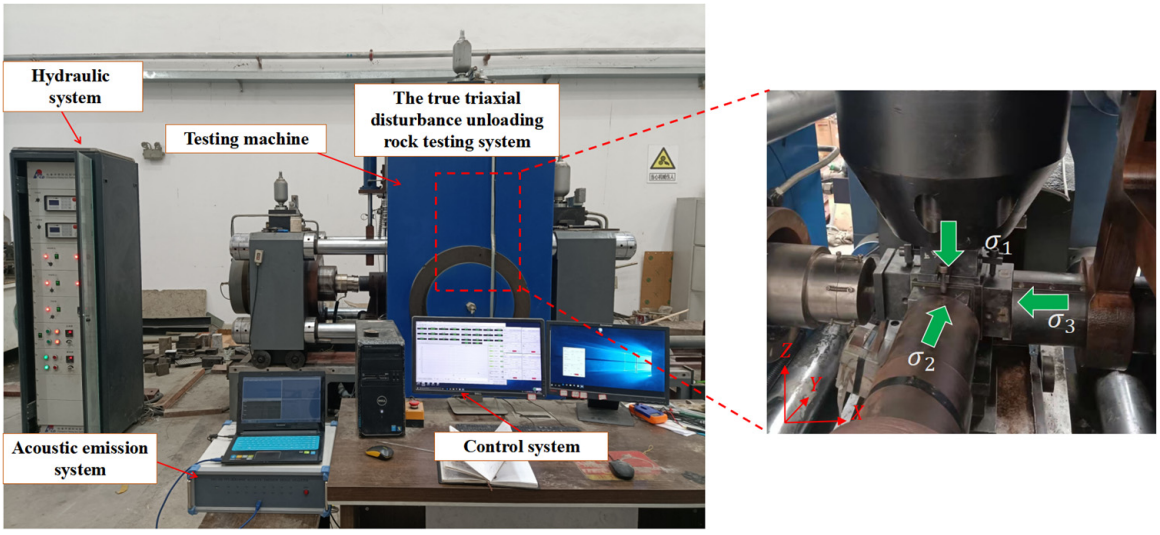

(**a**) Experimental system

Figure 2. *Cont.*

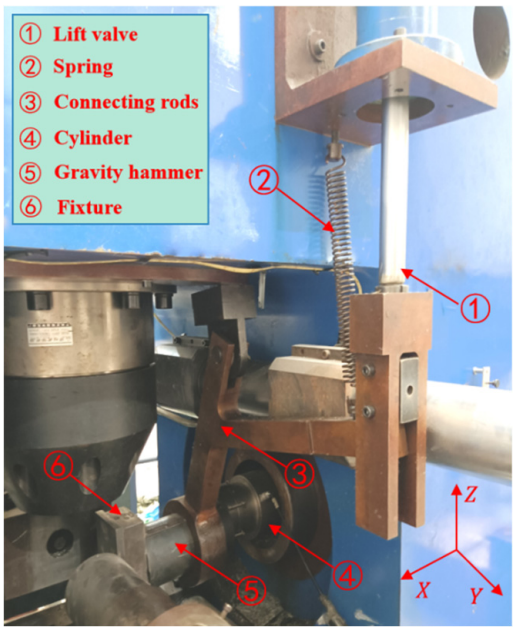

(**b**) Components of single-sided unloading

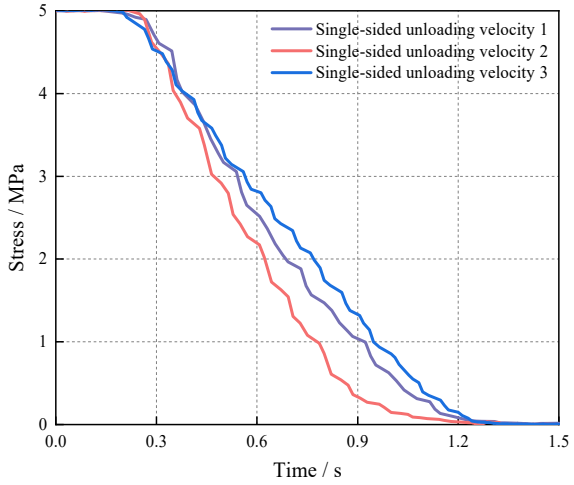

(**c**) Instantaneous single-sided unloading rate

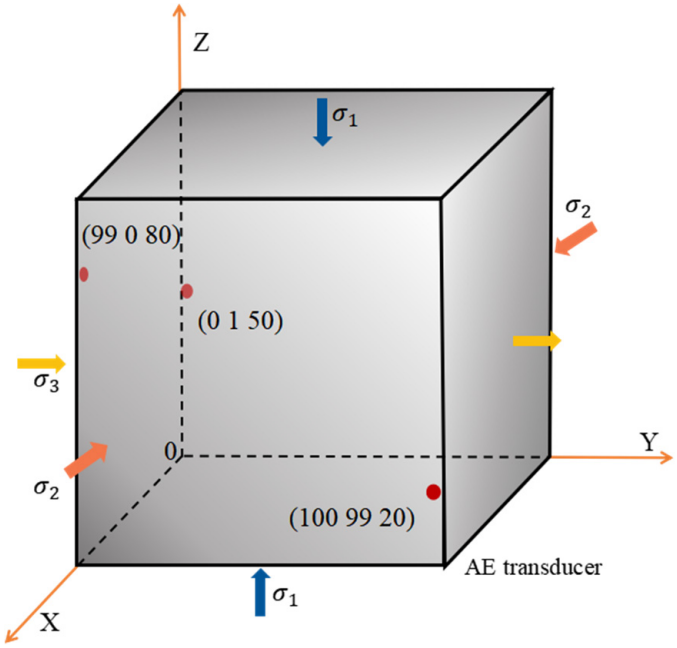

(**d**) AE transducer coordinate

Figure 2. True-triaxial test system for determining the characteristics of rock disturbance and unloading.

The above-described experimental set-up allowed us to simulate the stress state of the roadway surrounding rocks that changed from three-directional stresses acting on six faces to three-directional stresses on five faces due to sudden unloading. The stress-adjustment process of the shallow-lying element body in the roadway surrounding rocks was simulated. The unloading components are shown in Figure 2b.

Once the initial stress was reached during loading, ① was lifted before unloading. After the load imposed by ④ was removed, ⑥ plummeted down under the action of ⑤. Meanwhile, the elastic force of ② was imposed on ⑤ through ③. As a result, ⑥ was detached from the sample surface, and sudden unloading was achieved. The single-sided unloading was finished within an average time of 1.05 s.

The testing system was equipped with DS5-16B All-Information AE signal analyzer from Beijing Softland Company, Beijing, China, which recorded the ring-down count and AE energy throughout the tests. The acoustic emission preamplifier was 40 dB, the band-pass filter was 500 KHz, the hit definition time was 200 μs, the hit lockout time was 300 μs, the sampling frequency was 3 MHz, and the sampling time was synchronized with the beginning of the tester loading. The RS-54A broadband sensor from Beijing Softland Company, Beijing, China, was used, with a cylindrical diameter and height of 8 and 15.5 mm, respectively, and the coordinates of the transducer are shown in Figure 2d. A coupling agent was applied during installation to reduce friction. The monitoring results offered reliable measurements for the rock failure analysis.

2.3. Load Path for the Tests

During roadway excavation, the surrounding rocks shifted from in situ stress to unloading. That is, from being subjected to three-directional stresses on six faces to three-directional stresses on five surfaces. The radial stress acting on the surrounding rocks decreased in this process while the tangential stress increased [14]. The surrounding rocks failed as the concentrated stress exceeded the rocks' compressive strength (Figure 3a). The experimental load path for the true triaxial unloading tests was set up, as shown in Figure 3b, to simulate the transition of the stress state and analyze the law of influence of σ_2 on unloading in the sandstone samples. The samples were first subjected to true triaxial stresses. The loading rates in the directions of σ_1 and σ_3 were 60 kN/min and 10 kN/min, respectively. σ_2 would increase to the specified σ_2 within 5 min. Therefore, at σ_2 values of 5, 10, 15, 20, 25, and 30 MPa, the loading rates were 10, 20, 30, 40, 50, and 60 kN/min, respectively. With the σ_2 being constant, single-sided unloading was implemented instantaneously at σ_3. Then, the σ_1 was continuously increased at a 60 kN/min loading rate until rock failure.

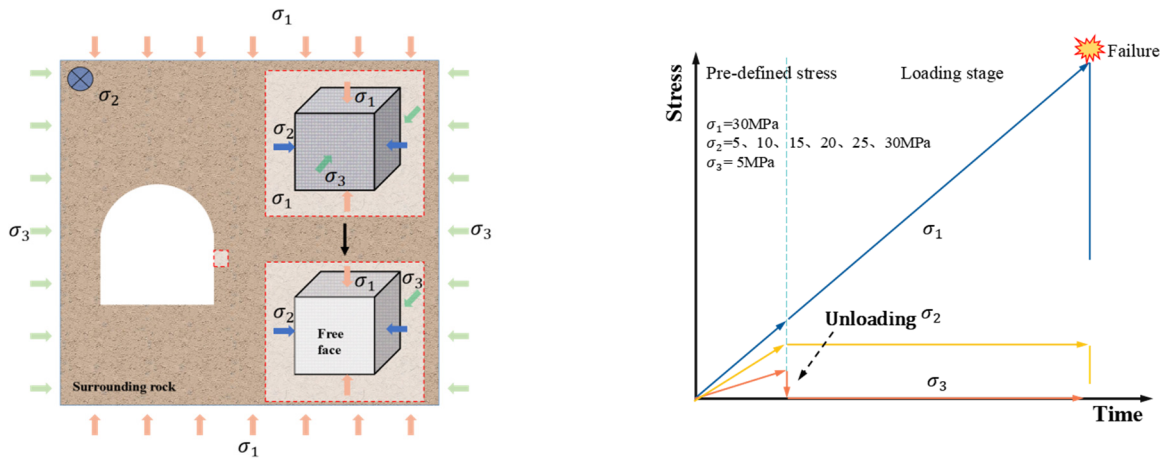

(**a**) Single-sided unloading process during the rock excavation (**b**) Unloading test paths

Figure 3. Unloading test paths for different intermediate principal stresses.

3. Experimental Results and Analysis

3.1. Mechanical Characteristics of Rocks in True Triaxial Unloading Tests

As the stress σ_2 varied, the rocks' strength and deformation characteristics under unloading differed significantly. We further analyzed the influence of single-sided unloading on the rocks' mechanical characteristics at different σ_2 values by plotting the stress–strain curves for the samples at different σ_2 values under unloading, as shown in Figure 4.

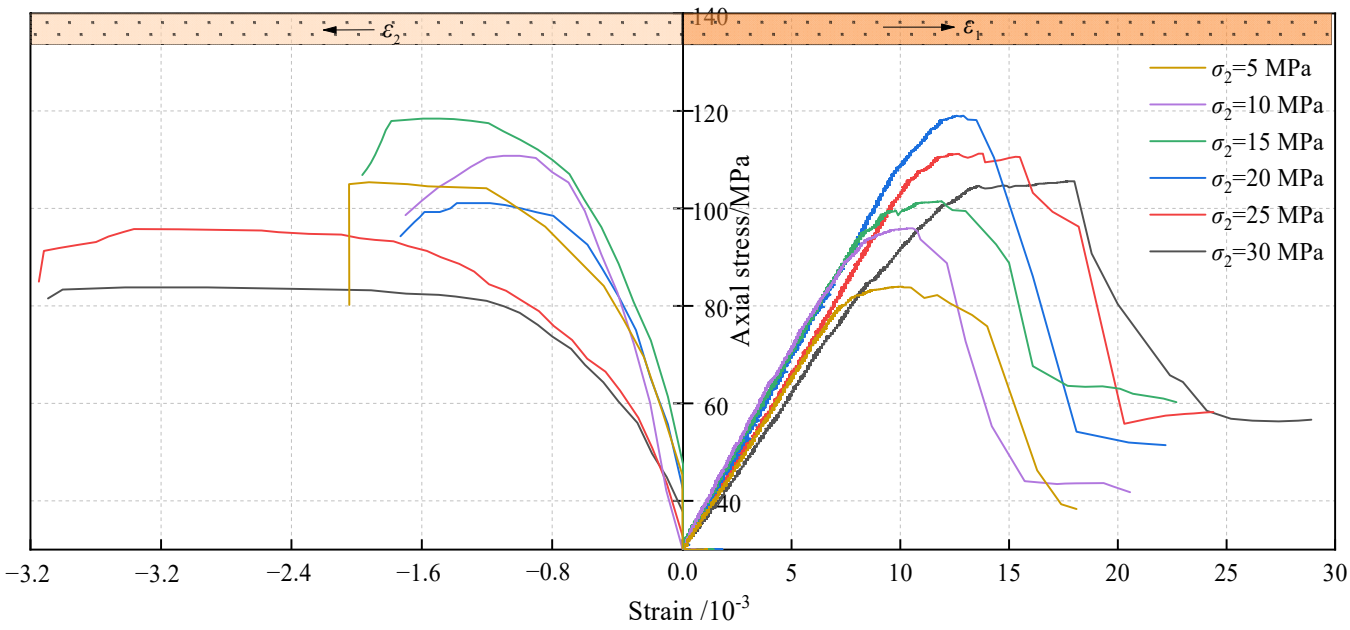

Figure 4. Stress–strain curves for different unloading specimens.

The results showed that the samples underwent axial rebound to varying degrees upon unloading, accompanied by a decreasing strain. The maximum variation of 1.80×10^{-3} was achieved at σ_2 = 20 MPa. During the loading process after unloading, the axial stress–strain curves showed an approximately linear trend, indicating axial compression. The rock samples were in an elastic state. The strain decreased in the direction of the second principal stress, and the volume expanded in the direction of σ_2 due to the continuously increasing axial stress. The strain $\Delta\varepsilon_2$ was estimated in the time interval between unloading and reaching 90% of the peak strength to quantify the rocks' ability to resist deformation. At σ_2 values of 5, 10, 15, 20, 25, and 30 MPa, the $\Delta\varepsilon_2$ values were 10.00×10^{-3}, 10.49×10^{-3}, 11.90×10^{-3}, 12.90×10^{-3}, 13.80×10^{-3}, and 18.00×10^{-3}, respectively. As the σ_2 increased, the strain $\Delta\varepsilon_2$ accommodated by the rock samples after unloading also increased. This means that σ_2 provided lateral support to the rocks under unloading, thereby enhancing the ability of the rocks to resist deformation under unloading.

At σ_2 values of 5, 10, 15, 20, 25, and 30 MPa, the peak strength values of the rock samples under single-sided unloading were 83.95, 95.93, 101.50, 119.00, 111.25, and 105.58 MPa, respectively. There was first an increase, followed by a decrease. The peak stress was the maximum at σ_2 = 20 MPa and reached the minimum at σ_2 = 5 MPa. This result indicates that the rocks' peak bearing capacity increased within a certain interval of stress concentration of σ_2. However, after σ_2 grew to a certain level, the local stress resulted in stress concentration, causing damage or even failure to the surrounding rocks. The bearing capacity of the rocks decreased gradually. Generally speaking, within the experimental range, the bearing capacity of the rocks under unloading grew when σ_2 grew from 0 to 20 MPa but decreased when it grew from 20 to 30 MPa. Hence, σ_2 initially had an enhancing effect, followed by a weakening effect on the bearing capacity of the surrounding rocks to some degree. Thus, σ_2 continuously strengthened the ability of the rocks to resist deformation under unloading.

3.2. Failure Characteristics of Rocks Under Unloading

The failure modes of the rocks were compared at different σ_2 points in the true triaxial unloading test. It can be seen in Figure 5 that the failure modes of the rocks differed significantly at different σ_2 values under unloading.

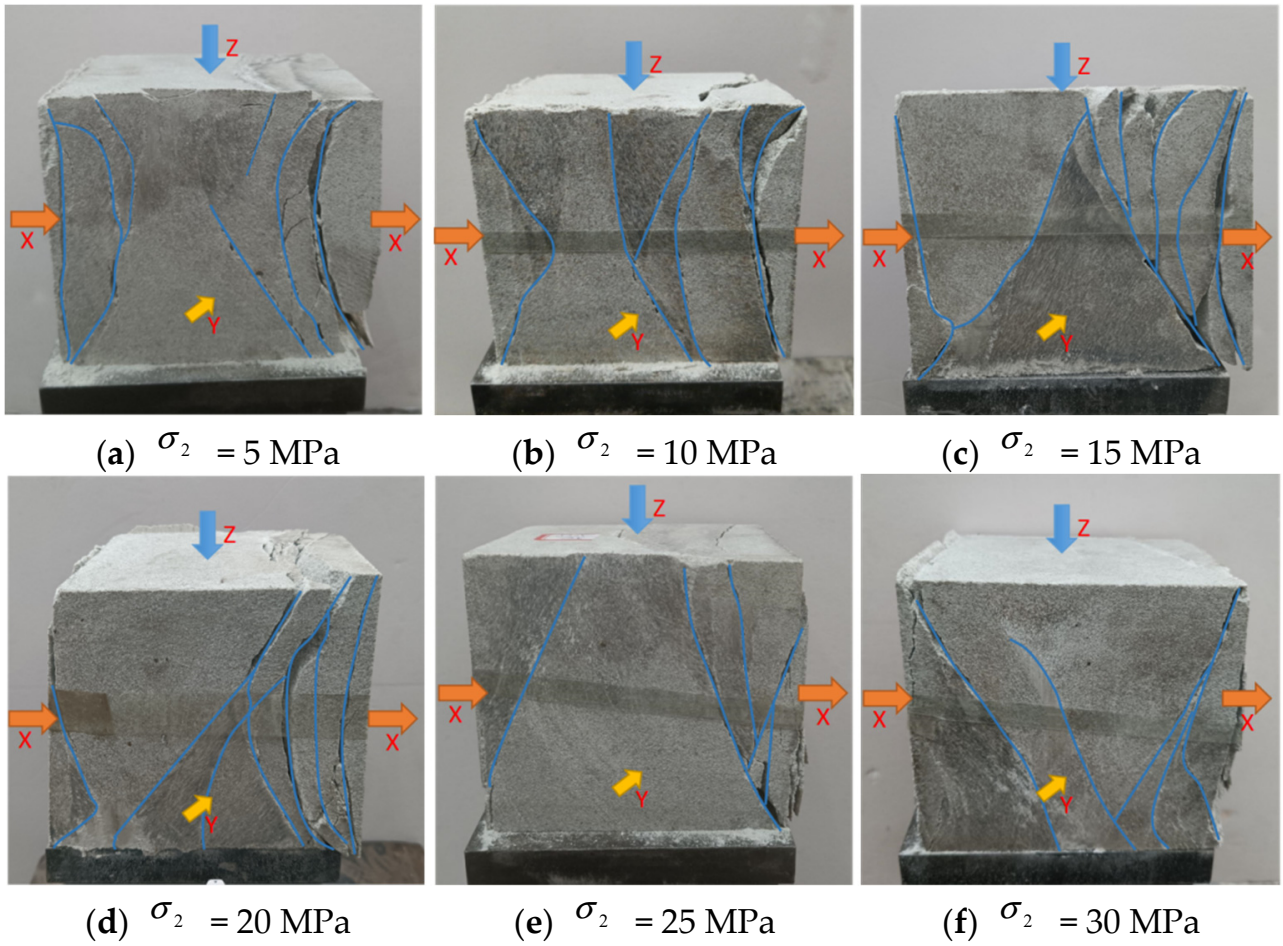

Figure 5. Damage pattern of different σ_2 unloading specimens.

At different σ_2 values, the principal fracture surfaces in the rocks due to unloading were approximately parallel with the direction of σ_2. At lower σ_2 values, the deformation was more serious along the x-direction, as was observed at σ_2 = 5 MPa. The principal fracture surfaces underwent a V-shaped failure due to compression-induced fracturing. Between the fracture surfaces, some penetrating oblique shear cracks appeared. No principal shear failure plane was observed despite the roughness between the fracture surfaces. As σ_2 gradually increased, the V-shaped fracture zone in the non-unloading face decreased in the x-direction. The arc radius of the V-shaped fracture zone increased, and oblique shear cracks were apparent. At σ_2 = 20 MPa, the more distinct layered fracture surfaces were due to compression-induced fracturing. No penetrating cracks appeared in the arc-shaped fracture surfaces near the unloading face. Greater smoothness was observed between the fracture surfaces than at σ_2 = 5 MPa. As σ_2 continued to increase to 30 MPa, the number and scope of the compression-induced fracture surfaces near the unloading face decreased compared with the situation at σ_2 = 20 MPa. The V-shaped fracture surface became more distinct but did not peel en bloc from the rock sample. Moreover, the non-unloading face in the x-direction did not show any distinct V-shaped fracture surface. The overall shear failure was easily identifiable.

Taken together, as σ_2 increased, the principal failure mode of the rock samples under unloading changed from tension failure to compound tension–shear failure and finally to shear failure. The number of cracks in the non-unloading face decreased in the x-direction. The number of layered fracture surfaces due to compression-induced fracturing near the free unloading face first increased and then decreased.

3.3. Failure Modes of Rocks Under Unloading

The overall failure mode of the rocks offers useful clues for the macroscopic control of surrounding rocks. However, the predominance of tension fracture did not necessarily mean that tensile cracks still dominated on the microscopic scale in the rocks under unloading. This study's microscopic failure mode of rocks under unloading was characterized quantitatively by the RA-AF ratio in the AE signals [31,32]. Based on our previous shear and Brazilian splitting tests [33], the RA-AF ratio was 380.

The RA-AF density cloud maps were plotted for the crack penetration process in rocks under unloading at different σ_2 values, as shown in Figure 6. The data points were denser as the color changed from red to blue. The data points were distributed over a larger area in regions with low RA and high AF. They were sparser and more dispersed in regions with high RA and low AF. Thus, the RA-AF density cloud map contained a triangular region. With σ_2 at 5 MPa, the number of tension cracks did not differ significantly from that of the shear cracks, with the latter being greater in number than the former by 10.06%. Although the tension cracks were more distinct macroscopically, shear failure was predominant on the microscopic scale during crack development and propagation. As a tension fracture surface was formed macroscopically, shear friction was caused by differences in the vertical deformation on the two sides of the failure planes.

The ratio of tension cracks to shear cracks under different σ_2 was counted and the results are shown in the circles of Figure 6. Within the experimental range, as σ_2 increased, the percentage of tension cracks first increased and then decreased, with the inflection point occurring at σ_2 = 15 MPa. The maximum percentage of tension cracks was 74.87%, which agreed with the macroscopic observation of the principal fracture cracks in the rocks under unloading. At σ_2 > 20 MPa, the percentage of tension cracks began to decrease. At σ_2 = 25 MPa, the percentage of tension cracks decreased to a similar level to that of shear cracks. The former value was 51.61%, indicating a slight predominance. At σ_2 = 30 MPa, the percentage of tension cracks was lower than that of shear cracks by 7.24%, indicating a slight predominance of the latter. As unloading-induced damage was caused to the rocks, the minimum percentage of tension cracks was 44.97%, while that of shear cracks was 25.13%. Due to the presence of a free unloading plane, the compression-induced tension cracks occurred extensively, and a varying σ_2 resulted in different percentages of failure modes. This further affected the maximum bearing capacity of the rocks. As σ_2 increased, the microscopic failure mode under unloading evolved from shear failure to tension failure and back to shear failure at the end.

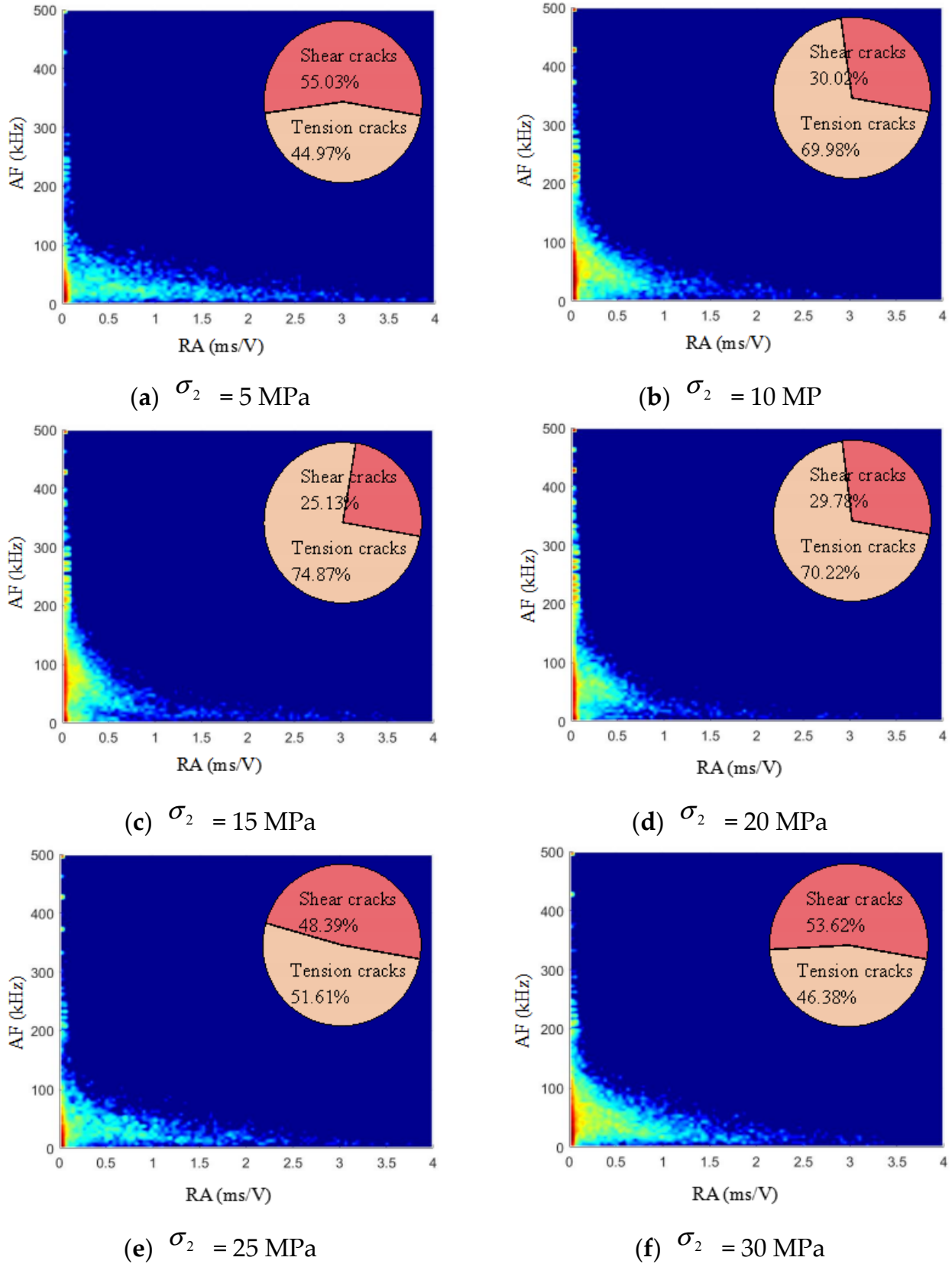

Figure 6. Density cloud plot of the RA-AF distribution.

3.4. Fractal Dimension of Rocks Under Unloading

The fractal dimension was estimated at different σ_2 values to describe the degree of crack development and the degree of rock failure. The fractal dimension of the coal–

rock composite samples increased along with the loading. This indicated that the cracks developed over time and communicated with each other until the failure plane was finally formed. The box dimension of the propagating cracks in the rocks under unloading was estimated at different σ_2 values. For this purpose, the regional division was performed using squares, and the crack propagation region was divided into an infinite number of squares, with side length r. The number of squares was $N(r)$. At $r \to 0$, the slope of the log–log graph of $N(r)$ vs. r was defined as the box dimension D. That is,

$$D = \lim \frac{\lg N(r)}{-\lg r} \tag{1}$$

where r, $N(r)$, and D are the side length of the square, the number of squares, and the fractal dimension of the cracks, respectively.

The calculation was performed using Matlab 2016. It can be inferred from Figure 7 that the sandstone samples' strength significantly influenced the failure morphology and crack evolution features in true triaxial unloading.

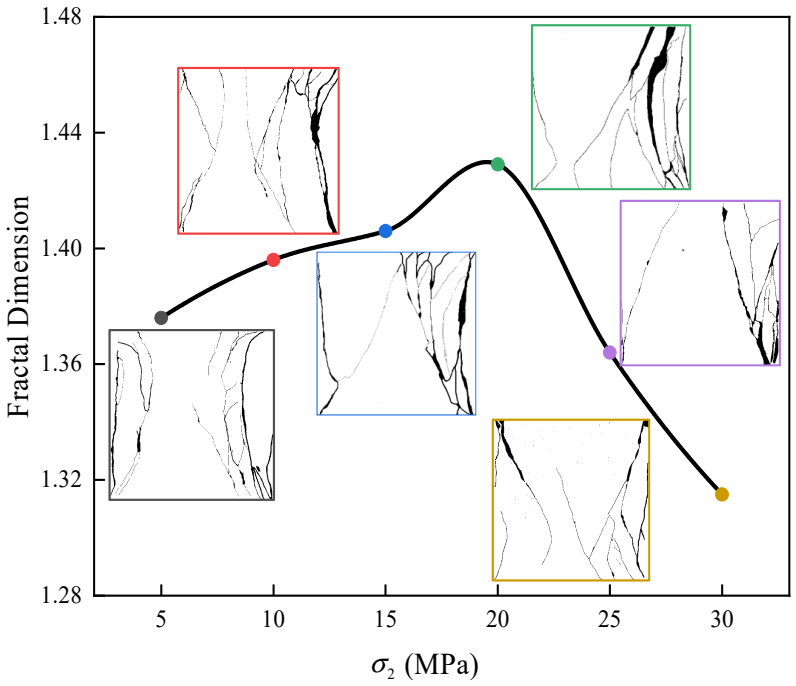

Figure 7. Fractal dimension of different intermediate principal stresses.

The fractal dimension was estimated based on the rock failure situation in Figure 3. The calculation showed that the crack development path and the propagation features varied significantly. The fractal dimensions were 1.383, 1.411, 1.421, 1.453, 1.374, and 1.326 at σ_2 values of 5, 10, 15, 20, 25, and 30 MPa, respectively. As σ_2 increased, the fractal dimension of the cracks first increased and then decreased. This variation trend was similar to that of the peak compressive strength of rocks. Moreover, the fractal dimension varied more slowly at $\sigma_2 < 20$ MPa than at $\sigma_2 > 20$ MPa. It was inferred that so long as σ_2 remained relatively small, an increase in σ_2 resulted in a higher bearing capacity of the rocks and more serious rock damage under unloading. The cracks were more developed, with the appearance of more short cracks. The crack density increased as well. That is, within the specified area, the cracks became denser and greater in number. The degree of crack development was the highest at 20 MPa, indicating the highest level of fracturing. But as σ_2 continued to increase, the rock damage weakened, inhibiting crack development. The

distribution of cracks became more concentrated, and the number of small cracks decreased, which indicated an inhibition of crack propagation.

4. Rock Failure Law and Multifractal Features

4.1. Evolution Pattern of Unloading-Induced Rock Failure

Two AE parameters, namely the ring-down count rate percentage (RCRP) and cumulative energy percentage (CEP), were defined to analyze the evolution law of AE signals during roadway surrounding rock failure in different stress states, as follows:

$$\mathrm{RCRP} = \frac{100N_i}{N_{\max}} \tag{2}$$

$$\mathrm{CEP} = \frac{100M_i}{M_{\max}} \tag{3}$$

where N_i and M_i are the values of RCRP and CEP at the point i, respectively. $N_{\max}$ and $M_{\max}$ are the maximum RCRP and CEP, respectively.

The features of the AE signals were analyzed statistically within the time interval from unloading to failure. Since time was linearly related to stress, the x-coordinates are normalized in Figure 8.

The AE signals at different σ_2 shared some similar features and were divided into four stages.

At stage II, the RCRP fluctuated mildly after unloading and intermittently, and the CEP changed slightly. In the surrounding rocks, the cracks densified and propagated.

At stage II, as the axial stress increased, the RCRP was persistently observable but remained very small, with intermittent jumps. The growth rate of the CEP gradually increased, accompanied by sudden increases by small margins. In this process, the fissures were communicated with each other to form cracks. It was inferred from the failure modes of the rocks in the above section that failure primarily occurred near the unloading plane.

At stage III, as the principal stress further increased, the RCRP was observable throughout the time period and remained high, with intermittent jumps by larger margins than at stage II. The growth rate of the CEP increased with sudden increases by larger margins. This feature was more pronounced at σ_2 values of 15 and 20 MPa. Before the jump in the RCRP, the RCRP first increased gradually until peaking and then decreased. The communication of the fracture surfaces near the unloading plane might cause the failure at this stage. However, a single failure event was insufficient to cause the overall instability of the rock samples under unloading.

At stage IV, as the failure events occurred in a jump-like manner more frequently, greater damage was caused to the rocks under unloading. The damage was more serious near the free unloading plane. The bearing structure of the rocks was gradually disrupted. Larger shear fracture surfaces were communicated with each other. The RCRP was persistently observable and remained high, with jumps. The growth rate of the CEP increased sharply, indicating an increase by a large margin.

Different features were observed and analyzed under varying intermediate principal stress. The percentage of released energy was also estimated to be 40% to 100% of the peak strength. The process was divided into stages T1 to T6 using a gradient defined as 10% of the peak strength, as shown in Figure 8. The CEP characterized the rock damage to some degree. At different σ_2 values, the CEP was smaller at T1, consistently below 3%. The CEP was always above 60% at T6, indicating that the major damage to the rocks primarily occurred at 90% to 100% of the peak strength (T6). As σ_2 increased, the percentages of released energy at T6 were 93.99%, 83.56%, 68.50%, 62.87%, 87.88%, and 90.13%, respectively. The initial decrease was followed by an increase, with the minimum

occurring at σ_2 = 20 MPa, a trend which was just the opposite of the variation of the peak strength of the rock samples under unloading. The above results revealed the change in the failure distribution pattern of the rocks, from being concentrated to dispersed and back to being concentrated again as σ_2 increased. More importantly, the fractal dimension increased and decreased, corroborating the above findings. The fractal dimension was the highest at σ_2 = 20 MPa, corresponding to the highest degree of rock fragmentation and the highest level of interactions between separate fracture surfaces.

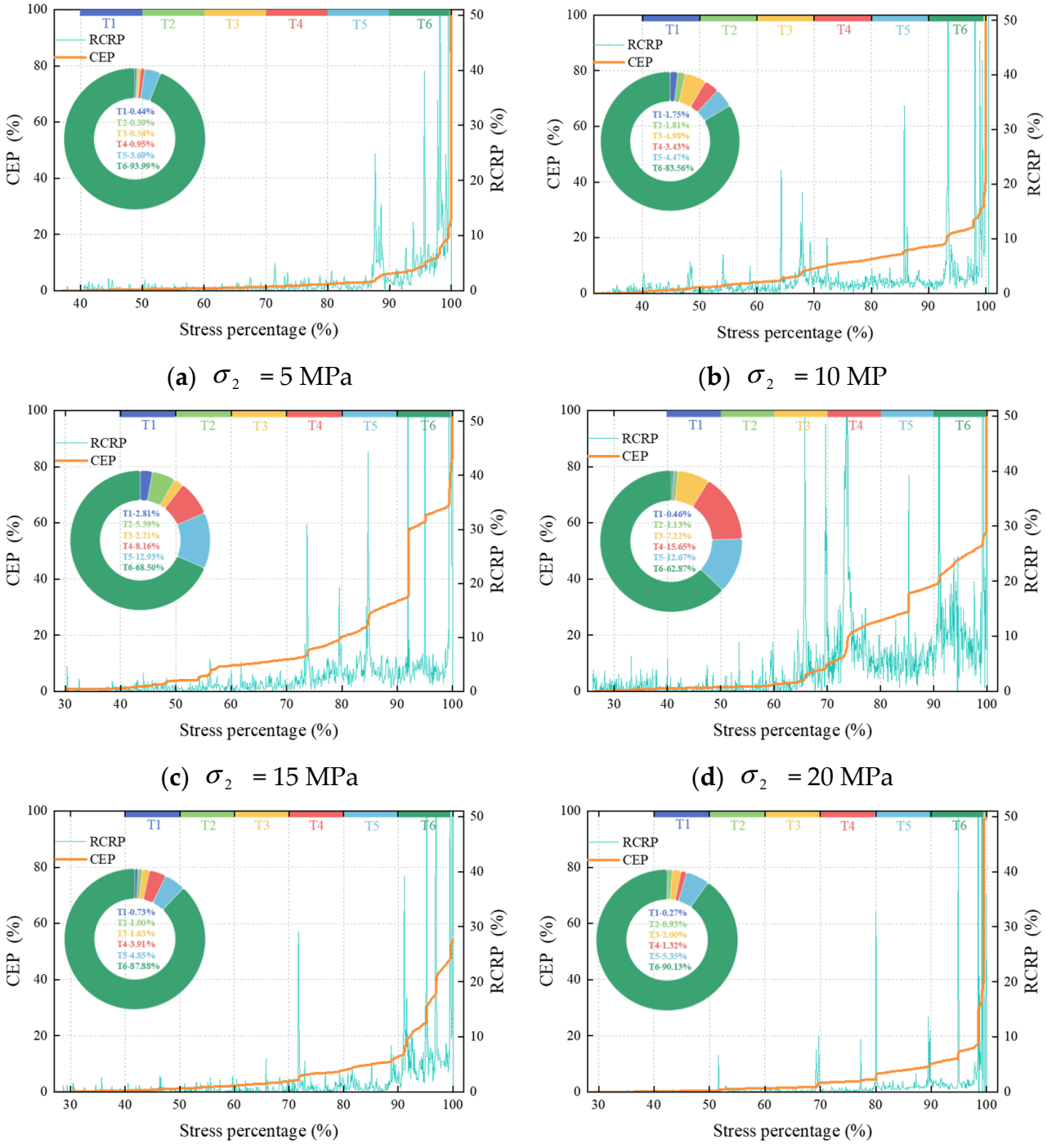

(**a**) σ_2 = 5 MPa (**b**) σ_2 = 10 MP

(**c**) σ_2 = 15 MPa (**d**) σ_2 = 20 MPa

(**e**) σ_2 = 25 MPa (**f**) σ_2 = 30 MPa

Figure 8. Temporal characterization of rock failure.

At σ_2 = 20 MPa, the RCRP remained high, from 65% to 95% of the peak strength, as shown in Figure 8d, and jumps occurred occasionally. This situation was more pronounced compared with other σ_2 values. At T4, the percentage of released energy exceeded 15.65%, while at other values of σ_2, the maximum percentage of released energy was only 8.16%. Therefore, major cracks appeared continuously at an earlier time at σ_2 = 20 MPa, while the major cracks occurred sporadically throughout the entire loading process.

The quantity of RCRP between 2% and 6% was estimated to quantify the degree of damage dispersion, as shown in Figure 9. Under the same percentage, the higher the quantity of RCRP being counted, the higher the degree of crack propagation or communication. As σ_2 increased, the quantity of RCRP being above 2% to 6% first increased and then decreased, with the inflexion point occurring at σ_2 = 20 MPa. The above results revealed that the number of rock failure events within the specified area first increased and then decreased, as σ_2 increased. The failure distribution was initially concentrated, then dispersed, and became concentrated again at the end.

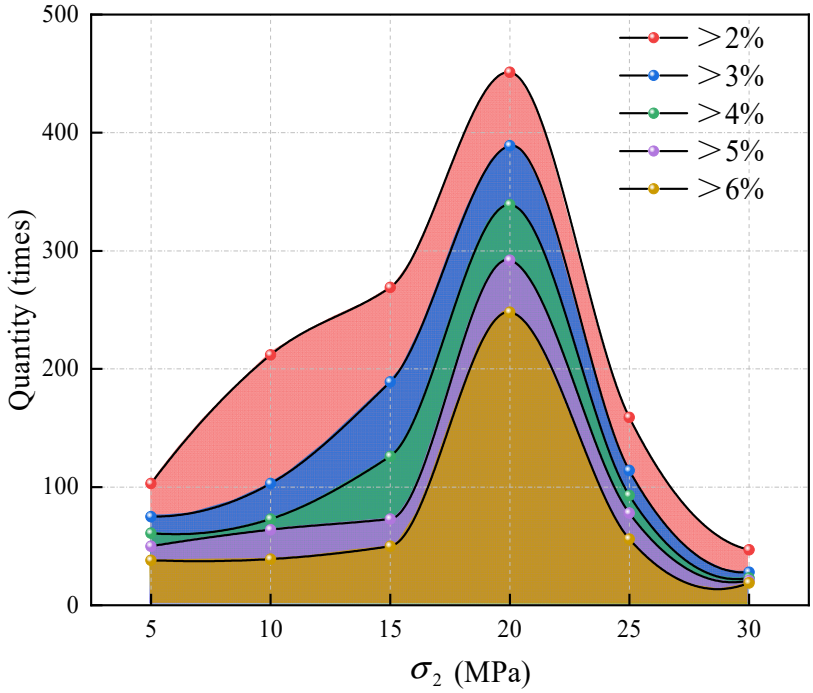

Figure 9. Characterization of the RCRP distribution under different σ_2 conditions.

4.2. Calculation Method for Multifractals of Ring-Down Count

The ring-down count fluctuated frequently in the time domain, and the data points were densely distributed. For this reason, the changes in the ring-down count only offer limited value for understanding the unloading-induced rock damage. Here, the multifractal theory was employed to study the distribution characteristics of the ring-down count from unloading to rock failure under different σ_2 values.

The box dimension is used to characterize the multifractal spectra of the time series [34]. The AE signal time series X are split into smaller interval X_i relative to the time scale δ. The normalized probability measure within each interval is $P_i(\delta)$. $N_i(\delta)$ is the cumulative sum in the local area.

$$P_i = N_i(\delta) \Big/ \sum_{i=1}^{x} N_i(\delta) \tag{4}$$

where $P_i(\delta)$ has a power law relationship with δ. α is the singularity index representing the singularity degree of the ring-down count distribution.

$$P_i(\delta) \sim \delta^{\alpha} \tag{5}$$

$$N_\alpha(\delta) \sim \delta^{-f(\alpha)} \tag{6}$$

where $f(\alpha)$ is the fractal dimension of the same subset α, which represents the variation of the ring-down count in the time domain. The estimation of $f(\alpha)$ and α requires building the partition function $Z_q(\delta)$. When the distribution of the ring-down count has multifractal features in the time domain, $Z_q(\delta)$ has a power law relationship with δ, as given by

$$Z_q(\delta) = \sum P_i(\delta) = \delta^{\tau(q)} \tag{7}$$

where q is the weight factor, and $\tau(q)$ is the quality index estimated from the slope of the $\ln Z_q(\delta) \sim \ln \delta$ curve.

For $\tau(q) - q$ representing the non-uniform distribution of the AE signals, the Legendre transformation is performed for $f(\alpha)$-α to obtain:

$$\alpha = [\tau(q) - \tau(q - \Delta q)]/\Delta q \tag{8}$$

$$f(\alpha) = \alpha q - \tau(q) \tag{9}$$

The calculation of the multifractal spectrum $\Delta\alpha$ and the corresponding $\Delta f(\alpha)$ yields

$$\Delta\alpha = \alpha_{\max} - \alpha_{\min} \tag{10}$$

$$\Delta f(\alpha) = f(\alpha_{\max}) - f(\alpha_{\min}) \tag{11}$$

where $\alpha_{\min}$ and $\alpha_{\min}$ correspond to high- and low-energy signals, respectively; while $\Delta f(\alpha)$ represents the difference between the percentages of $\alpha_{\min}$ and $\alpha_{\min}$ in the entire time domain.

Furthermore, the generalized fractal dimension D_q is introduced to describe the multifractal features of the ring-down count distribution in the time domain. The generalized fractal dimension D_q and $\tau(q)$ are related as follows:

$$D_q = \begin{cases} t'(1) & q = 1 \\ \frac{t(q)}{q-1} & q \neq 1 \end{cases} \tag{12}$$

4.3. Analysis of Multifractal Features of Ring-Down Count

The multifractal spectra of the ring-down count were obtained at σ_2 values from unloading to rock failure, as shown in Figure 10. The multifractal spectra at different σ_2 values shared similar shapes. Function $f(\alpha)$ first increased and then decreased as α grew.

The spectra curved rightwards and downwards after hitting the highest point, indicating distinct fractal features during the sandstone failure. The width of the multifractal spectrum $\Delta\alpha$ quantified the contrast between the maximum and the minimum probability subsets in the fractals. That is, the degree of differentiation of the ring-down data. The larger the $\Delta\alpha$, the more non-uniform the ring-down count distribution in the time domain and the more violent the fluctuations would be. The polarization trend was conspicuous.

It can be seen that the fractal spectra' width differed slightly, indicating differences in the multifractal features, while $\Delta f(\alpha)$ was consistently positive at different σ_2, suggesting that the frequency of low ring-down data points was higher in the time domain. At σ_2 values of 5, 10, 15, 20, 25, and 30 MPa, the $\Delta\alpha$ values were 1.506, 1.227, 1.180, 1.054, 1.121,

and 1.420, respectively. It can be observed that as σ_2 increased, $\Delta\alpha$ first decreased and then increased. $\Delta\alpha$ was the maximum at σ_2 = 5 MPa, corresponding to the largest difference in the ring-down count distribution after unloading. It can be seen in Figure 8 that the RCRP began to increase only beyond 87% of the peak stress and in a significant manner. This resulted in polarization of the distribution pattern and more concentrated failure distribution. $\Delta\alpha$ was the maximum at σ_2 = 5 MPa, corresponding to the smallest difference in the ring-down count distribution after unloading. The ring-down count distribution was also more uniform. $\Delta\alpha$ first decreased and then increased as σ_2 increased, indicating that the failure distribution was initially concentrated in the rocks under unloading, then became more uniform, and was concentrated at the end. The variation agreed well with the findings from the previous studies.

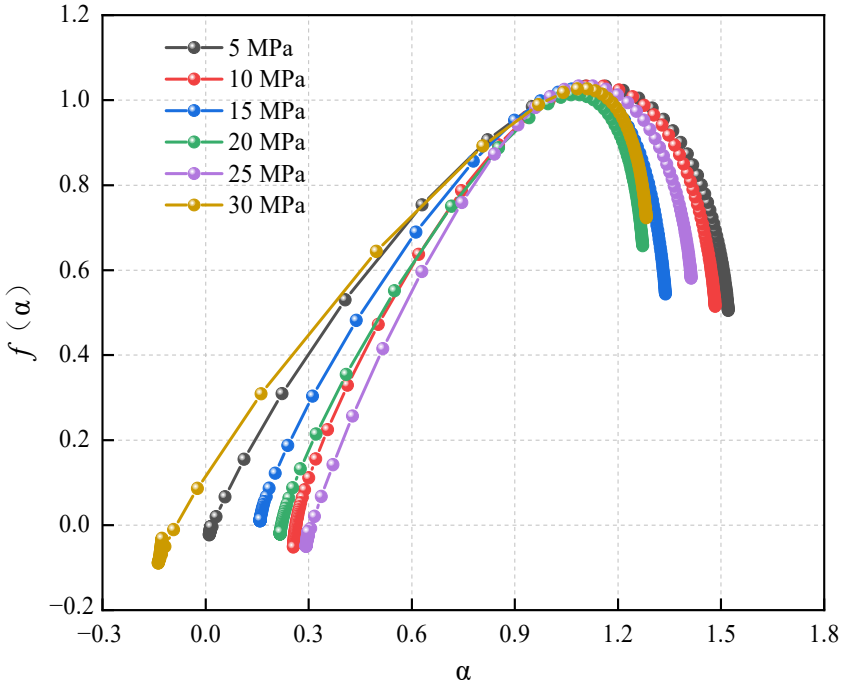

Figure 10. Singular spectrum spectra of multifractals for different σ_2.

The evolution of the relationship between q and D_q was analyzed based on the ring-down counts from 40% (T1) to 100% (T6) of the peak damage. It can be seen in Figure 11 that q were D_q non-linearly related. D_q decreased gradually as q increased, indicating the multifractal features of the ring-down count distribution and the irregularity of the distribution. As the damage became more serious, the generalized dimension D_q changed significantly. It can be found from Figure 12 that at stage T6, where rock failure happened, the non-linear relationship between D_q and q was enhanced. D_q showed a greater degree of divergence and, hence, stronger multifractal features. The above results suggest that the distribution of the ring-down count became increasingly less uniform in the time domain, and the crack propagation within the samples became much more discontinuous. This was a portent of the impending rock failure due to unloading.

The capacity dimension D_0 and the information dimension D_1 represented the slopes at $f(q)$ at q values of 0 and 1, respectively. The average values of D_0/D_1 from T1 to T6 were used to characterize the uniformity of the ring-down count distribution in the time domain. The closer the value to 1, the more uniform the distribution and the weaker the fractal features would be. D_0/D_1 was extracted at different σ_2, and the comparison is shown in Figure 12. It can be found that as σ_2 increased, D_0/D_1 first decreased and then increased. The non-uniformity of the ring-down count distribution in the time domain first decreased

and then increased. Small crack propagation was predominant at a lower σ_2, while sudden, large cracks were predominant at a higher σ_2. The failure distribution displayed a higher level of non-uniformity.

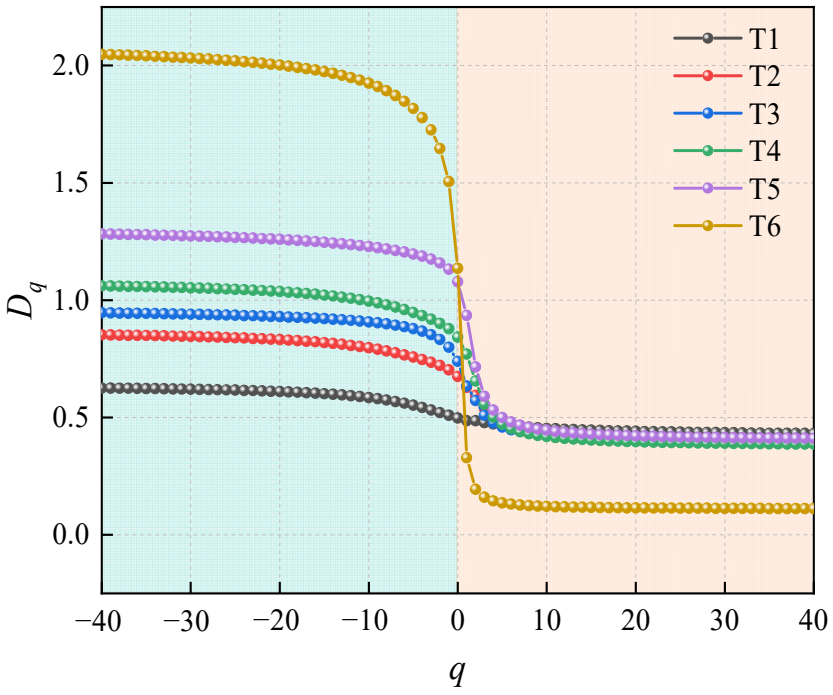

Figure 11. Generalized dimensional spectral D_q-q curve for σ_2 = 30 MPa.

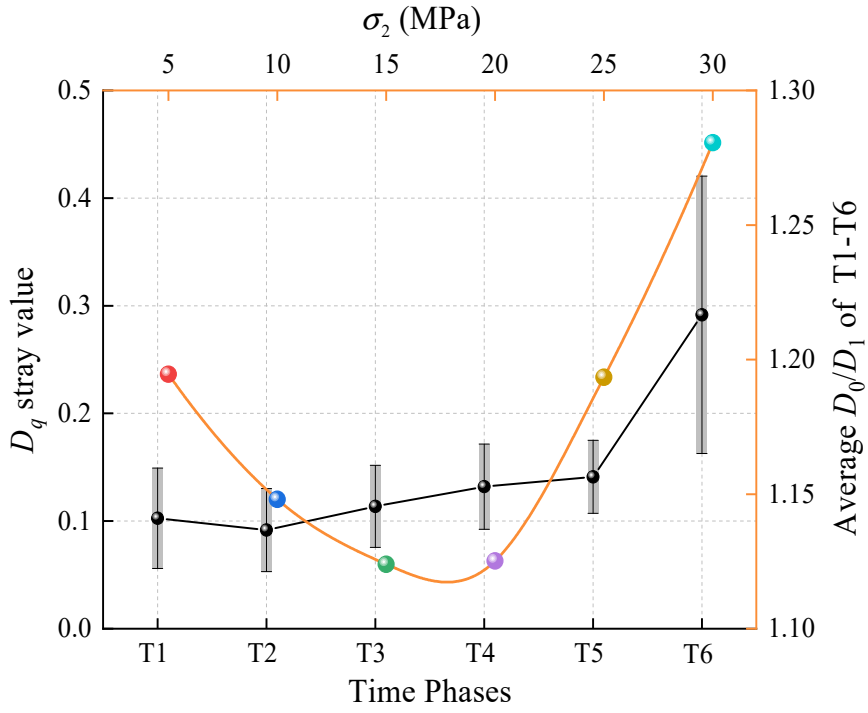

Figure 12. Variation of the ringing count dimension information for different σ_2 and stages.

5. Discussion

Other studies have not yet reported an initial increasing trend of the peak strength of rocks, followed by a decrease at a later time, in the presence of an intermediate principal stress based on experimental findings [4,6,7,14]. Nevertheless, our results agree with

those of Lu [35] and Song [36]. Analyzing the variation curve of the peak strength of rocks provides informative guidance for real-world applications. In the present study, the Lorentz function had a high goodness-of-fit for non-linear and convergent data. The data analysis is shown in Figure 13, and the peak strength was well correlated with σ_2 in the rocks under unloading. It can be observed from the fitted curve that the inflection point in the peak strength of the rocks under unloading was about 21.82 MPa. We could roughly estimate the peak bearing capacity of the rocks within a certain range at different σ_2 under unloading. It is noteworthy that according to previous studies, σ_2 is about 21.5 MPa when the burial depth of the roadway is 1200 m. Therefore, the inflection point for the influence of σ_2 on the roadway may occur at a burial depth of about 1200 m. This finding sheds some light on engineering design and highlights need to enhance the bearing capacity of the surrounding rocks by appropriately increasing σ_2. It is also necessary to prevent higher levels of fragmentation and energy release due to an increased σ_2.

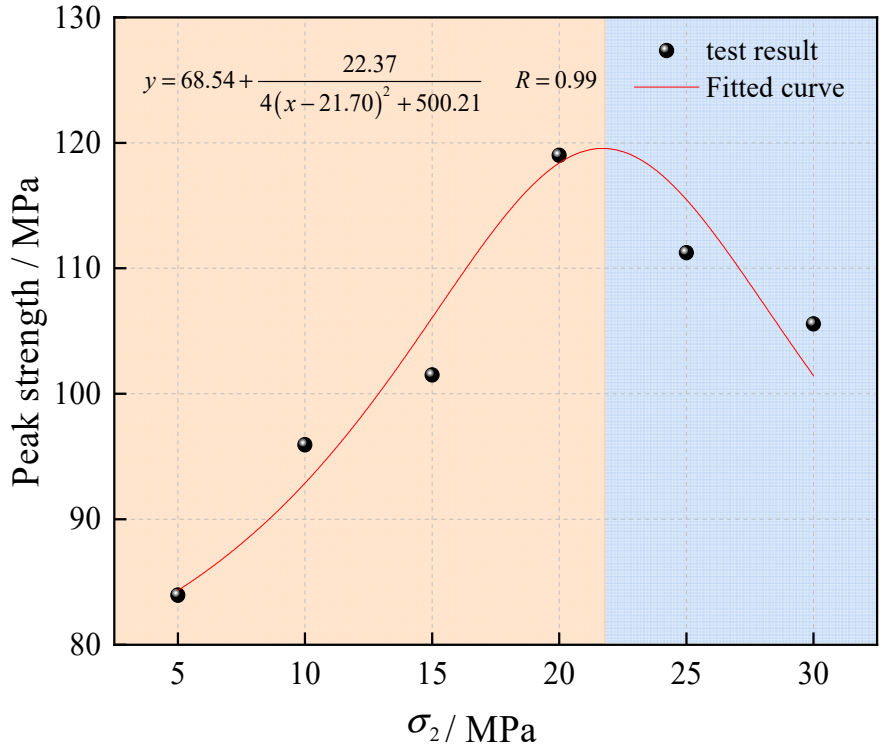

Figure 13. Variation of the peak strength of different unloading specimens.

Some new insights can be gained by analyzing the experimental findings. According to engineering practices in surrounding rock control, although increasing σ_2 can enhance the bearing capacity of the surrounding rocks, the cracks within may develop more significantly after failure, making the surrounding rock control even more difficult. Based on our experimental findings, the fractal dimension was higher at a smaller σ_2, accompanied by a larger number of cracks and more frequent tension failure events. Efforts should be made to restore the radial stress in the surrounding rocks using anchor bolts and I-beams.

More importantly, as σ_2 increased, the failure distribution pattern was initially concentrated, then dispersed, and became concentrated again at the end. Considering the results of the fractal dimension D and RCRP, for example, at T6 with σ_2 = 30 MPa, an increasing D_0/D_1 caused a concentrated distribution of shear failure and the communication of large fracture surfaces. It is necessary that we strengthen the internal friction in the surrounding rocks and their shear capacity by grouting and using shear bolts to prevent high-energy shear failure due to stress concentration.

6. Conclusions

True triaxial unloading tests were performed on sandstone samples at different σ_2 using the true triaxial unloading rock test system and the AE monitoring system. The mechanical response and failure characteristics of the sandstone at different σ_2 were revealed. The multifractal and singular spectra of the AE signals representing sandstone failure were analyzed. We arrived at the following conclusions:

(1) An increasing σ_2 first had an enhancing effect and then a weakening effect on the bearing capacity of the surrounding rocks to some degree. However, its continuous increase strengthened the ability of the rocks to resist deformation under unloading.

(2) As σ_2 increased, the principal failure mode of the rock samples under unloading changed, macroscopically, from tension failure to compound tension–shear failure and finally to shear failure. Microscopically, the predominant failure mode changed from shear failure to tension failure and finally to shear failure. The fractal dimension of the cracks first increased and then decreased.

(3) Major damage caused to the rocks under unloading primarily occurred at T6. The number of rock failure events within the specified area first increased and then decreased, as σ_2 increased. The failure distribution was initially concentrated, then dispersed, and became concentrated again at the end.

(4) The multifractal spectra of the ring-down count initially showed an increasing trend and then a decrease over time. The spectra curved rightwards and downwards after hitting the highest point. As σ_2 increased, the fractal dimension $\Delta\alpha$ of the cracks in the rocks first increased and then decreased. The failure distribution of the rocks under unloading was initially concentrated, became more uniform, and was concentrated again at the end. D_0/D_1 first decreased and then increased. The non-uniformity of the ring-down count distribution in the time domain first decreased and then increased.

Author Contributions: C.L., conceptualization, methodology, formal analysis, writing—original draft; C.P. and W.X., investigation, data curation, formal analysis, writing—review and editing; G.Z. and X.M., resources, writing—review and editing, project administration, funding acquisition, supervision. All authors have read and agreed to the published version of the manuscript.

Funding: This research was funded by the Scientific Research Foundation for High-level Talents of Anhui University of Science and Technology, China (No. 2023yjrc131), the Open Research Grant of Joint National-Local Engineering Research Centre for Safe and Precise Coal Mining, China (No. EC2023026), the National Key Research and Development Project of China (No. 2023YFC2907600), and the National Natural Science Foundation of China (Nos. 52404068 and 52004006).

Data Availability Statement: The data produced and/or evaluated in this study can be obtained from the corresponding author upon request.

Conflicts of Interest: The authors declare no conflicts of interest.

References

1. Cai, M.; Brown, T. Challenges in the mining and utilization of deep mineral resources. *Engineering* **2017**, *3*, 432–433. [CrossRef]
2. Liu, C.; Zhao, G.; Pan, C.; Meng, X.; Xu, W.; Liu, W. Damage analysis and grading control technology of surrounding rock in high geo-stress roadway. *Sci. Rep.* **2025**, *15*, 1188.
3. Si, X.; Luo, Y.; Gong, F.; Huang, J.; Han, K. Temperature effect of rockburst in granite caverns: Insights from reduced-scale model true-triaxial test. *Geomech. Geophys. Geo-Energy Geo-Resour.* **2024**, *10*, 26.
4. Mogi, K. Fracture and flow of rocks under high triaxial compression. *Geophys. Res.* **1971**, *76*, 1255–1269. [CrossRef]
5. Si, X.; Luo, Y.; Luo, S. Influence of lithology and bedding orientation on failure behavior of "D" shaped tunnel. *Theor. Appl. Fract. Mech.* **2024**, *129*, 104219.
6. Liu, C.; Zhao, G.; Xu, W.; Meng, X.; Huang, S.; Zhou, J.; Wang, Y. Experimental investigation on failure process and spatio-temporal evolution of rockburst in granite with a prefabricated circular hole. *J. Cent. South Univ.* **2020**, *27*, 2930–2944.

7. Haismon, B.; Chang, C. A new true triaxial cell for testing mechanical properties of rock, and its use to determine rock strength and deformability of Westerly granite. *Int. J. Rock Mech. Min. Sci.* **2000**, *37*, 285–296.
8. Li, Z.; Wang, L.; Wang, L.; Fan, H.; Ren, B.; Ding, K. Study on the evolution of rock fracture under true triaxial intermediate principal stress. *Int. J. Geomech.* **2024**, *24*, 04023254.
9. You, W.; Dai, F.; Liu, Y.; Du, H.; Jiang, R. Investigation of the influence of intermediate principal stress on thedynamic responses of rocks subjected to true triaxial stress state. *Int. J. Min. Sci. Technol.* **2021**, *31*, 913–926. [CrossRef]
10. Takahashi, M.; Park, H.; Takahashi, N.; Fujii, Y. True triaxial tests–using permeability and extensional stress parameters to simulate geological history in rocks. *Geosyst. Eng.* **2013**, *16*, 75–82. [CrossRef]
11. Feng, X.; Kong, R.; Zhang, X.; Yang, C. Experimental Study of Failure Differences in hard rock under true triaxial compression. *Rock Mech. Rock Eng.* **2019**, *52*, 2109–2122. [CrossRef]
12. Chang, X.; Zhang, X.; Dang, F.; Zhang, B.; Chang, F. Failure behavior of sandstone specimens containing a single flaw under true triaxial compression. *Rock Mech. Rock Eng.* **2022**, *55*, 2111–2127.
13. Li, X.; Feng, F.; Li, D.; Ranjith, P.; Roatami, J. Failure characteristics of granite influenced by sample height-to-width ratios and intermediate principal stress under true-triaxial unloading conditions. *Rock Mech. Rock Eng.* **2018**, *51*, 1321–1345.
14. Liu, C.; Zhao, G.; Xu, W.; Meng, X.; Liu, Z.; Cheng, X.; Lin, G. Experimental study on failure characteristics of single-sided unloading rock under different intermediate principal stress conditions. *Int. J. Min. Sci. Technol.* **2023**, *33*, 275–287.
15. Li, W.; Wang, Z.; Zhang, H.; Du, J.; Li, H.; Duan, M. Dilation and energy evolution mechanisms of sandstone under true-triaxial mining unloading conditions. *Geomech. Geophys. Geo-Energ. Geo-Resour.* **2024**, *10*, 58.
16. Dong, C.; Fan, C.; Lu, X.; Zhao, G.; Qi, M.; Qin, R. Mechanical and energy evolution characteristics of sandstone under true triaxial cyclic loading. *Appl. Sci.* **2023**, *13*, 7230. [CrossRef]
17. Jiang, B.; Gu, S.; Wang, L.; Zhang, G.; Li, W. Strainburst process of marble in tunnel-excavation-induced stresspath considering intermediate principal stress. *J. Cent. South Univ.* **2019**, *26*, 984–999. [CrossRef]
18. Pan, C.; Liu, C.; Zhang, G.; Yuan, W.; Wang, X.; Meng, X. Fractal Characteristics and energy evolution analysis of rocks under true triaxial unloading conditions. *Fractal Fract.* **2024**, *8*, 387. [CrossRef]
19. Luo, Y.; Huang, J.; Si, X.; Wu, W.; Li, S. Failure characteristics and energy properties of red sandstone under uniaxial compression: Water content effect and its application. *Bull. Eng. Geol. Environ.* **2025**, *84*, 57.
20. Zhang, Z.; Zhang, R.; Xie, H.; Liu, J.; Were, P. Differences in the acoustic emission characteristics of rock salt compared with granite and marble during the damage evolution process. *Environ. Earth Sci.* **2015**, *73*, 6987–6999.
21. Zhang, Q.; Meng, X.; Zhao, G. Energy evolution and fractal characteristics of sandstones under true triaxial cyclic loading and unloading. *Fractal Fract.* **2024**, *8*, 714. [CrossRef]
22. Zhang, H.; Wang, Z.; Song, Z.; Zhang, Y.; Wang, T.; Zhao, W. Acoustic emission characteristics of different brittle rocks and its application in brittleness evaluation. *Geomech. Geophys. Geo-Energ. Geo-Resour.* **2021**, *7*, 48. [CrossRef]
23. Li, D.; Wang, E.; Kong, X.; Wang, X.; Zhang, C. Fractal characteristics of acoustic emissions from coal under multi-stage true-triaxial compression. *J. Geophys. Eng.* **2018**, *15*, 2021–2032.
24. Zhao, K.; Song, Y.; Yan, Y.; Gu, S.; Wang, J.; Guo, X.; Luo, C.; Suo, T. Mechanics and acoustic emission fractal characteristics of surrounding rock of tantalum-niobium mine under splitting condition. *Nat. Resour. Res.* **2022**, *31*, 149–162. [CrossRef]
25. Zhang, Y.; Liu, Y.; Tao, Z.; Zhou, H.; Yang, Q. Fractal Characteristics and failure analysis of geomechanical model for arch dam based on acoustic emission technique. *Int. J. Geomech.* **2019**, *19*, 11. [CrossRef]
26. Kantelhardt, J.W.; Zschiegner, S.A.; Koscielny-Bunde, E.; Havlin, S.; Bunde, A.; Stanley, H.E. Multifractal detrended fluctuation analysis of nonstationary time series. *Phys. A* **2002**, *316*, 87–114. [CrossRef]
27. Xie, X.; Li, S.; Guo, J. Study on multiple fractal analysis and response characteristics of acoustic emission signals from goaf rock bodies. *Sensors* **2022**, *22*, 2746. [CrossRef]
28. Cai, J.; Chen, Y.; Zhang, D. Study on the feature of acoustic emission of rock under compression experiment based on multi-fractal theory. *Chin. J. Undergr. Space Eng.* **2012**, *8*, 963–968.
29. Lu, Y.; Kang, P.; Yang, L.; Hu, X.; Chen, H. Multi-scale characteristics and gas-solid interaction among multiple beds in a dual circulating fluidized bed reactor system. *Chem. Eng. J.* **2020**, *385*, 123715. [CrossRef]
30. Feng, X.; Haimson, B.; Li, X.; Chang, C.; Ma, X.; Zhang, X.; Ingra-ham, M.; Suzuki, K. ISRM suggested method: Determining deformation and failure characteristics of rocks subjected to true triaxial compression. *Rock Mech. Rock Eng.* **2019**, *52*, 2011–2020. [CrossRef]
31. Ohno, K.; Ohtsu, M. Crack classification in concrete based on acoustic emission. *Constr. Build. Mater.* **2010**, *24*, 2339–2346.
32. Ohtsu, M. Recommendations of RILEM Technical Committee 212-ACD: Acoustic emission and related NDE techniques for crack detection and damage evaluation in concrete: Test method for classification of active cracks in concrete structures by acoustic emission. *Mater. Struct.* **2010**, *43*, 1187–1189.
33. Liu, C.; Pan, C.; Zhao, G.; Xu, W.; Meng, X. Experimental study on the failure mechanism of roadway surrounding rock under true triaxial loading: Insights from acoustic emission (AE) characteristics. *Measurement* **2025**, *31*, 116727. [CrossRef]

34. Grassberger, P. Generalized dimensions of strange attractors. *Phys. Lett. A* **1983**, *97*, 227–230.
35. Lu, J.; Xie, H.; Li, M.; Li, C.; Gao, M.; Shang, D.; Li, J. Effect of microwave radiation on mechanical behaviors of tight fine sandstone subjected to true triaxial stress. *Int. J. Rock Mech. Min. Sci.* **2022**, *152*, 105063.
36. Song, Z.; Ying, G. Influence of the intermediate principal stress on sandstone failure. *Rock Mech. Rock Eng.* **2019**, *52*, 3033–3046.

Disclaimer/Publisher's Note: The statements, opinions and data contained in all publications are solely those of the individual author(s) and contributor(s) and not of MDPI and/or the editor(s). MDPI and/or the editor(s) disclaim responsibility for any injury to people or property resulting from any ideas, methods, instructions or products referred to in the content.